Interfacial optimization for AlN/diamond heterostructures via machine learning potential molecular dynamics investigation of the mechanical properties

*Zijun Qi [1, 2, #], Xiang Sun [1, 2, #], Zhanpeng Sun [1, 2], Qijun Wang [1, 2], Dongliang Zhang [3], Kang Liang [1, 2], Rui Li [1, 2], Diwei Zou [2], Lijie Li [5], Gai Wu [1, 2, *], Wei Shen [1, 2, 4, *], Sheng Liu [1, 2, 3]*

[1] The Institute of Technological Sciences, Wuhan University, Wuhan, 430072, China

[2] School of Power and Mechanical Engineering, Wuhan University, Wuhan, 430072, China

[3] School of Mechanical Science and Engineering, Huazhong University of Science and Technology, Wuhan, 430074, China

[4] Hubei Key Laboratory of Electronic Manufacturing and Packaging Integration, Wuhan University, Wuhan, 430072, China

[5] College of Engineering, Swansea University, Swansea, SA1 8EN, UK

[*] Corresponding Authors:

Gai Wu, E-mail: wugai1988@whu.edu.cn

Wei Shen, E-mail: wei_shen_@whu.edu.cn

[#] Zijun Qi and Xiang Sun contributed equally to this work.

KEYWORDS: AlN/diamond heterostructure; Neuroevolution machine learning potential; Molecular dynamics; Interfacial mechanical property; Interfacial structure optimization

ABSTRACT

AlN/diamond heterostructures hold tremendous promise for the development of next-generation high-power electronic devices due to their ultrawide bandgaps and other exceptional properties. However, the poor adhesion at the AlN/diamond interface is a significant challenge, which will lead to film delamination and device performance degradation. In this study, the uniaxial tensile failure of the AlN/diamond heterogeneous interfaces has been investigated by molecular dynamics simulations based on a neuroevolutionary machine learning potential (NEP) model. The interatomic interactions can be successfully described by the trained NEP, the reliability of which has been demonstrated by the prediction of the cleavage planes of AlN and diamond. It can be revealed that the annealing treatment can reduce the total potential energy by enhancing the binding of C and N atoms at interfaces. The strain engineering of AlN also has an important impact on the mechanical properties of the interface. Furthermore, the influence of the surface roughness and the interfacial nanostructures on the AlN/diamond heterostructures has been considered. It can be indicated that the combination of surface roughness reduction, AlN strain engineering and annealing treatment can effectively result in superior and more stable interfacial mechanical properties, which can provide a promising solution to the optimization of mechanical properties of ultrawide bandgap semiconductor heterostructures.

1. INTRODUCTION

Emerging ultra-wide bandgap (UWBG) semiconductor materials, represented by aluminum nitride (AlN), diamond and gallium oxide (Ga_2O_3), exhibit excellent properties and have attracted significant interest for their exceptional characteristics and the potential applications in electronics,[1,2]

optoelectronics,[3] thermal management,[4,5] and surface acoustic wave (SAW) devices.[6] The band gaps of AlN and diamond are 6.2 eV and 5.5 eV, respectively, and their ultrawide bandgaps and large breakdown electric field can further improve the efficiency and power density of the high-power and high-frequency electronic devices.[7] AlN has a theoretical thermal conductivity of 319 $W \cdot m^{-1} \cdot K^{-1}$, surpassing that of most semiconductor materials such as Si, GaN, and Ga_2O_3. Diamond is considered the ultimate semiconductor material with a thermal conductivity as high as 2000 $W \cdot m^{-1} \cdot K^{-1}$.[8] Due to the excellent physical properties, AlN/diamond heterostructures have been regarded to be one of the most promising solutions for the thermal management challenge in high-frequency and high-power devices.

As the buffer layer and thermal management function layer, the AlN/diamond heterostructures can optimize the growth quality and the heat dissipation performance of III-nitrides, such as the AlGaN/GaN/AlN heterostructures which are widely used for the fabrication of high-electron mobility transistors and deep-ultraviolet light-emitting diode devices.[9-12] Besides, as for thin film devices, the AlN/diamond heterostructures have been developed for light-emitting diodes and field-effect transistors.[13-16] However, one major challenge for AlN/diamond heterostructures is the poor interfacial adhesion,[17] which may result in the film delamination and subsequently the performance and reliability degradation for thin film devices. During heterogeneous epitaxial growth using methods such as microwave plasma chemical vapor deposition and metal organic chemical vapor deposition, significant temperature differences occur during deposition, coupled with the mismatch of thermal expansion coefficient between the materials, resulting in a large stress. The development of surface activated bonding (SAB) technology can offer a promising solution to this challenge, which enables room-temperature bonding.[18] Additionally, annealing treatment following SAB is also beneficial for further optimization of bonded structure.[19] Strain, like temperature, is an integral component of the material phase diagram and has a crucial influence on the regulation of material properties.[20] Its impact extends to material stability,[21] band structure,[22] and ferroelectricity,[23] thus catalyzing advancements in the field of strain engineering. Although the AlN/diamond

heterostructures have been extensively studied in the fabrication process as well as the thermal properties in the previous research efforts,[5, 24-28] the mechanical properties of the heterogeneous interfaces between AlN and diamond still remain unexplored, because it is really challenging for the direct observation and description of the interfacial failure mechanisms of the heterostructures through the experimental methods. Molecular dynamics (MD) simulations can provide a methodology for in-depth study of interfacial interactions, and tensile strain simulations can furthermore reveal the mechanisms of structural evolution under various influencing factors, including crystal structure, thermal transport, tensile and compressive stresses. Previous researchers have developed various interatomic potentials to describe AlN and diamond individually.[29-34] Nonetheless, a specialized interatomic potential that can accurately describe the interaction between AlN and diamond is lacking. The introduction of machine learning potentials (MLPs) offers a novel approach to develop an interatomic potential. MLPs have demonstrated remarkable accuracy, which are comparable to that of the density functional theory (DFT) calculations, and can also significantly enhance the simulation efficiency and scalability.[35-37] Fan et al. developed a neuroevolution machine learning potential (NEP) model.[34, 38-40] Compared to other MLPs, the NEP improves efficiency of simulation calculations, even approaching the performance of embedded atom method potentials.[35, 41]

In this paper, the NEP model is utilized to investigate the optimization strategies of the interfacial adhesion strength between AlN and diamond in heterostructures. In section 2, the NEP training and computational methods are briefly introduced. In section 3, the results of NEP training and MD simulations are shown and discussed. This part includes the accuracy assessment of NEP, tensile simulations, and the effect of annealing, AlN strain engineering and interfacial morphology on heterogeneous interface adhesion. The key findings are summarized in the concluding section.

2. COMPUTATIONAL DETAILS

2.1. AIMD calculations

The ab initio molecular dynamics (AIMD) calculations in this study were conducted using the Vienna Ab initio Simulation Package (VASP) based on density functional theory.[42-43] The electron-ion interaction and exchange correlation functional were characterized using the projected augmented wave (PAW) method and the generalized gradient approximation (GGA) with the Perdew-Burke-Ernzerhof (PBE) functional.[44-45] The single Γ point in the Brillouin zone was sampled and the energy cutoff was set as 550 eV. A 1 fs time step was applied, and the electronic self-consistency convergence criterion was set to 10^{-6} eV. The AIMD calculations were performed using the NVT ensemble, which allowed the temperature to float within a certain range for rich sampling, and the basic models included block, surface, vacancy structures, and AlN/diamond heterostructures. The lattice constants of diamond and wurtzite structure AlN were a_C = 3.574 Å and a_{AlN} = 3.128 Å, respectively. As shown in Figure 2a, the variations of strain (0.90-1.14) and temperature (18 K-2027 K) were imposed on the block model, the atomic numbers of AlN and diamond were 128 and 64 (without vacancy), respectively. The AlN/diamond heterostructures with different crystal orientation combinations were explored, with AlN(0001)/diamond(100) model and AlN(0001)/diamond(110) model containing 512 atoms and AlN(0001)/diamond(111) model containing 328 atoms.

2.2. Neuroevolution machine learning potential training

The AIMD calculations of AlN, diamond, and AlN/diamond heterostructures resulted in 10,710 structures, which were constructed into the total dataset. The NEP training was conducted in two rounds. In the first round, a training dataset and a test dataset were established based on the total dataset in a 4:1 ratio, consisting of 8,568 and 2,142 structures, respectively. The fourth version of NEP model from the GPUMD package was applied to train the NEP model for AlN/diamond heterostructures.[34, 39-40] The NEP model employed a single-layer neural network (NN) to compute the energy, force, and virial values of the structures. Throughout iterations under hyperparametric control, the root mean square error (RMSE) between the NEP-predicted values and the DFT calculation values continuously converged, ultimately resulting in a potential with exceptional predictive performance. The hyperparameter settings for NEP-AlN/diamond training could be presented in Table 1. In contrast

to the NEP-Carbon model,[34] this work extended the radial and angular cutoffs to 5 Å to enhance potential accuracy. The hidden layer contained 50 neurons, and the batch size was set at 1000. Different from the default parameters, the force weight in the loss function (λ_f) was increased from 1.0 to 2.0, while the virial weight (λ_v) was raised from 0.1 to 0.5 as previous work had confirmed the significance of virial in predicting the elastic properties and heat transport prediction.[34] After the initial round of NEP training, the obtained potential was utilized to reselect the training and testing datasets from the original dataset by PyNEP, an active learning package for NEP. The final training dataset consisted of 846 structures, while the test dataset included 9,864 structures, and then the second round of NEP training employed the same hyperparameters as the first round.

Table 1. Hyperparameters for the NEP of AlN/diamond heterostructure.

Parameter	Value	Parameter	Value
r_C^R	5 Å	r_C^A	5 Å
n_{max}^R	8	n_{max}^A	8
N_{basis}^R	10	N_{basis}^A	10
l_{max}^{3b}	4	l_{max}^{4b}	2
l_{max}^{5b}	0	λ_1	0.05
λ_2	0.05	λ_e	1.0
λ_f	2.0	λ_v	0.5
N_{neuron}	50	N_{batch}	1000
$N_{population}$	60	$N_{generation}$	300000

2.3. Tensile model in molecular dynamics simulations

Molecular dynamics simulations were carried out by GPUMD,[40] using the trained NEP to describe the interaction between the atoms. Periodic boundary conditions were applied in all three dimensions, and the time step was set as 1 fs. Initially, all models underwent isothermal-isobaric (NPT) ensemble simulation at 300 K for 100 ps, employing the Bernetti-Bussi barostats.[46] And then, uniaxial strain was applied to the model via incrementally increasing the simulation box length in the *z*-direction at each time step (Figure 1a-c). After testing, a strain rate of 5×10^7 s^{-1} was selected for subsequent simulations, which can be regarded as quasi-static loading.

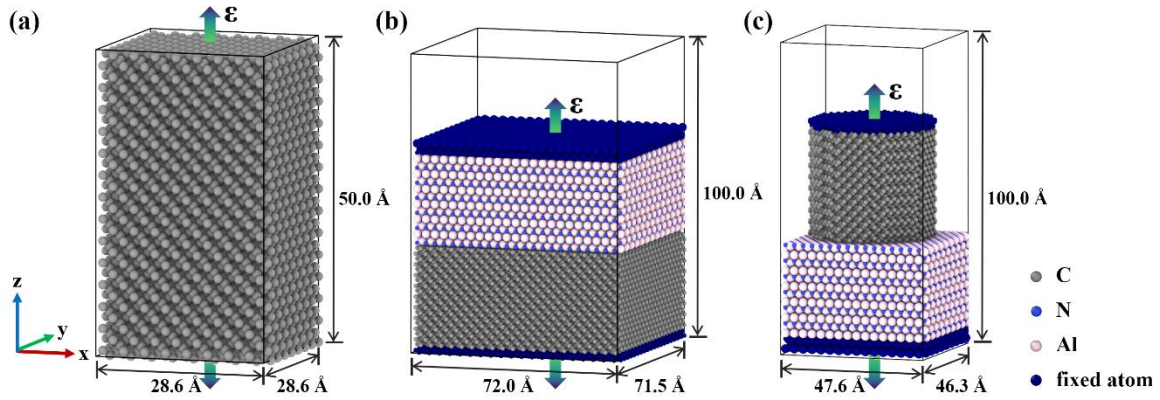

Figure 1. Models for calculating the uniaxial tensile stress-strain curves (a) diamond model, (b) AlN-diamond heterostructures model, and (c) heterogeneous nanopillar model.

To investigate the tensile properties of the AlN/diamond heterostructure, a variety of AlN/diamond heterogeneous models have been constructed, in which the interfaces contained different combinations of crystal orientations, and the dimensions of these models were about 70 × 70 × 100 $Å^3$. Additionally, the models of diamond nanopillars on AlN bulk have been constructed, where the AlN bulk had various tensile-compressive strains (0.95-1.05) in the *xy*-plane by scaling the lattice constant of AlN and controlling the simulation box size. As shown in Figure 1b,c, the vacuum layer was introduced to eliminate the influence of non-study object interfaces on tensile simulations. After relaxation, the velocity and force of the atoms at the ends of both diamond and AlN were set to 0. Subsequently, the length of the simulation box was increased to achieve the uniaxial tensile simulations of the AlN/diamond heterogeneous models. In the annealing treatment, the models were annealed in the temperature range of 500 K to 1900 K. All temperature controls remained in the NPT ensemble with the additional processes including heating up to the annealing temperature for 100 ps, the relaxation at the specified temperature for 100 ps, and cooling to 300 K for 100 ps.

3. RESULTS AND DISCUSSION

3.1.Training and validation of the NEP

The variation of each loss function with the number of iterations during the second round of NEP training has been illustrated in Figure 2a. The loss functions for energy, force, and virial reached

convergence after approximately 3×10^5 iterations at the end of the training process. The predicted values generated by NEP (Figure 2c-e) show good consistency with the calculated values of DFT for both the training and test datasets. The final root mean square errors (RMSEs) for energy, force, and virial are 1.64 meV/atom, 113.42 meV/Å, and 22.90 meV/atom in the training dataset and are 1.59 meV/atom, 110.38 meV/Å, and 20.89 meV/atom in the test dataset. After the first round of NEP training, the structures selected in the second round of training form a smaller training dataset but a more even distribution of coverage across energy, force and virial, which could enhance the accuracy and stability of MD simulations with NEP.

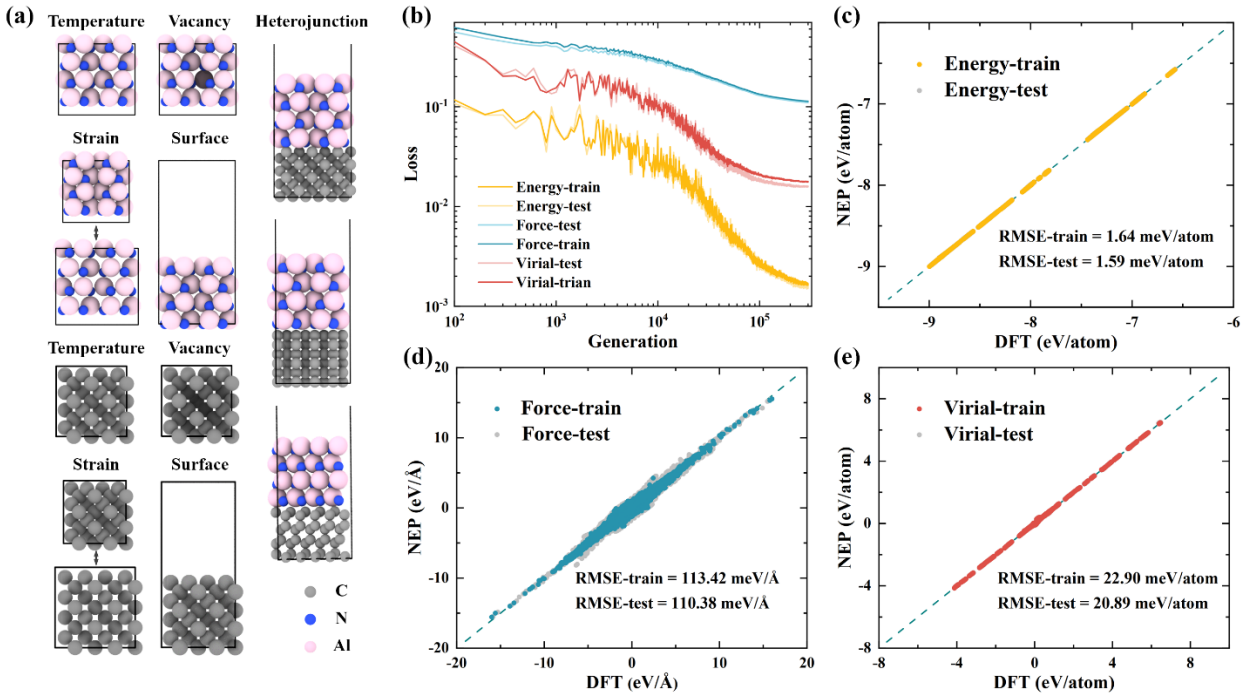

Figure 2. (a) Models for ab initio molecular dynamics calculations.(b) Evolution of various loss functions with respect to generations. (c) Energy, (d) force and (e) virial calculated by NEP and DFT in the training and test datasets.

Pair distribution functions (PDFs) are pivotal for assessing the precision of interatomic potentials. Figure 3a,b give the comparison of PDFs using various methods, including DFT, NEP, and the Tersoff potential, with simulation conducted at a temperature of 300 K. The g(r) curve of AlN calculated by NEP agrees well with the DFT results. In contrast, the g(r) curve calculated by the Tersoff potential exhibits a slight leftward shift compared to the DFT calculations, with the difference becoming more noticeable at greater pair distances. The g(r) curves for diamond calculated by the three methods are

all in good agreement. These PDF results indicate that NEP has successfully achieved consistency with DFT in characterizing the structural properties of AlN and diamond. Furthermore, the trained NEP proves to be more accurate than the conventional Tersoff potential when describing AlN. To confirm the reliability of the NEP predictions in strained systems, a series of block structures have been generated with strain sizes ranging from 0.9 to 1.1 at intervals of 0.1 by modifying the lattice constants. The system energy calculated through the NEP prediction is highly consistent with the DFT calculations (Figure 3c,d). In the heterogeneous model system, the potential energies predicted by NEP with different interface distances also show good consistency with DFT (Figure S1).

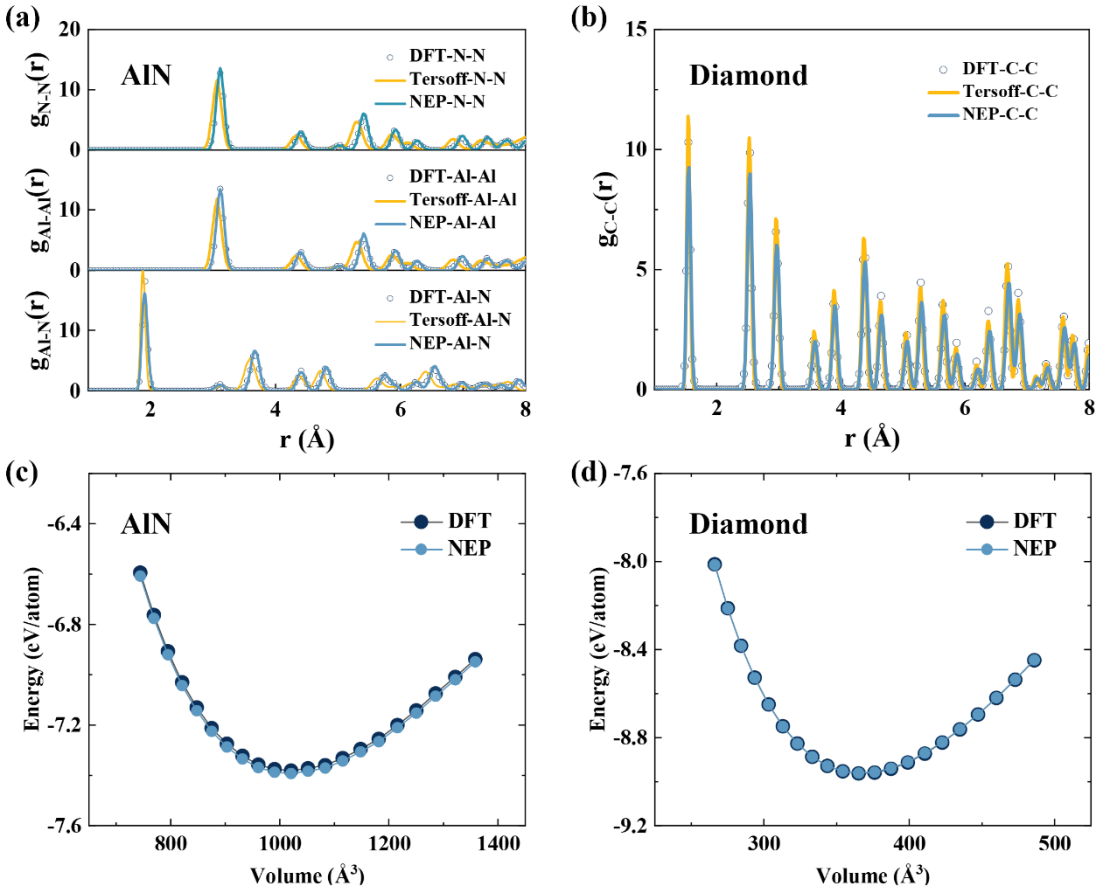

Figure 3. Radial distribution functions for (a) AlN and (b) diamond calculated by DFT (hollow dots), NEP (blue lines), and Tersoff (yellow lines). The energy-volume (E-V) curves for (c) AlN and (d) diamond calculated by DFT (dark blue dots) and NEP (light blue dots).

3.2. Uniaxial tensile simulations

The results of uniaxial tensile simulations for diamond along the [100], [110], and [111] directions combined with AlN along the [0001] direction are shown in Figure 4, and the calculation

of the effect of model size on tensile simulation is provided in Figure S2 of the Supporting Information. The results have been visualized and analyzed using the OVITO program, while the Identify Diamond Structure method has been employed to identify cubic/hexagonal diamond structure atoms and surface atoms.[47] The diamond tensile fracture predicted by NEP is predominantly along the (111) plane (Figure 4a-c), which is consistent with the experimental diamond cleavage plane.[48-49] Similarly, the simulated tensile fracture surfaces of AlN correspond to the (0001) plane (Figure 4d), in alignment with the cleavage plane of AlN. For diamond, the tensile fracture strength in the [100], [110], and [111] directions are 149 GPa, 99 GPa, and 86 GPa, respectively, which are close to the experimental results.[48] The tensile fracture strength of AlN in [0001] direction is 34 GPa, which agrees with the previous reference.[50] A strain of 0.01 has been used in the calculation of tensile modulus, resulting in the modulus values of 874 GPa for diamond along the (100) direction and 301 GPa for AlN along the (0001) direction. Comparing these modulus values to the experimental results,[48, 51] the modulus results predicted by our NEP potential appear relatively small. Nonetheless, this NEP potential effectively captures the tensile fracture process and the trends in stress-strain curves, particularly in predicting fracture surfaces that align with actual crystal cleavage phenomena, which emphasizes the advantages and reliability of this potential.

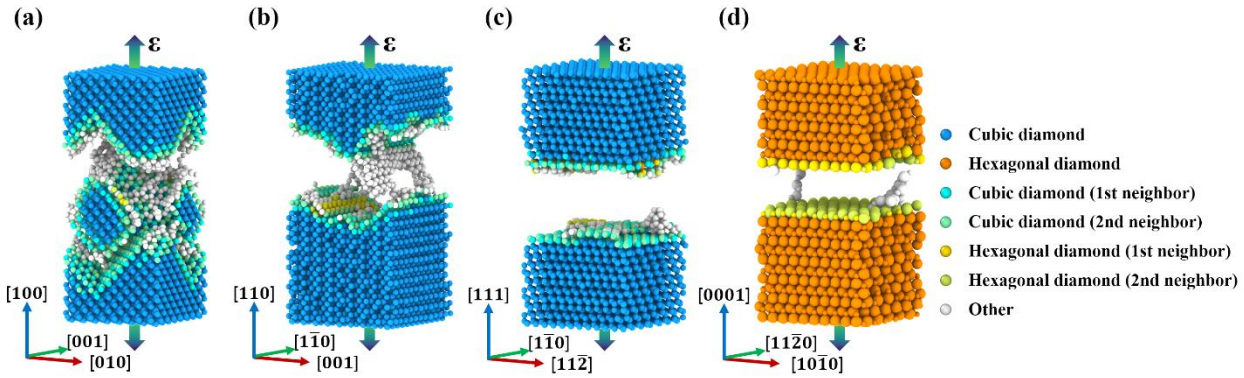

Figure 4. Uniaxial tensile fracture models for (a) diamond [100], (b) diamond [110], (c) diamond [111], and (d) AlN [0001].

Figure 5a displays the tensile stress-strain curves for AlN/diamond heterostructure, where the (0001) plane of AlN is combined with the (100), (110), and (111) planes of diamond. Among these diamond planes combined with AlN, the (100) and (111) planes exhibit higher stress and strain values

upon fracture, indicating stronger interfacial adhesion compared to the (110) plane. The (111) plane demonstrates a slightly larger modulus, while the (100) plane exhibits the most robust interfacial performance, with fracture stress and strain values of 15.5 GPa and 0.065, respectively. The strain distribution reveals that the fractures of the AlN(0001)/diamond(100) and AlN(0001)/diamond(111) heterostructures both initiate from a void defect in AlN near the interface. The void defect leads to stress concentration and triggers the cleavage of the AlN(0001) plane in a short time. As a result, the heterostructures fracture and leave a layer of AlN on the diamond. However, the heterogeneous fracture of the AlN(0001)/diamond(110) has no process of AlN cleavage, but instead direct detachment and delamination at the interface, indicating that the binding of AlN and diamond atoms at the interface is not as strong as that of the (100) and (111) planes.

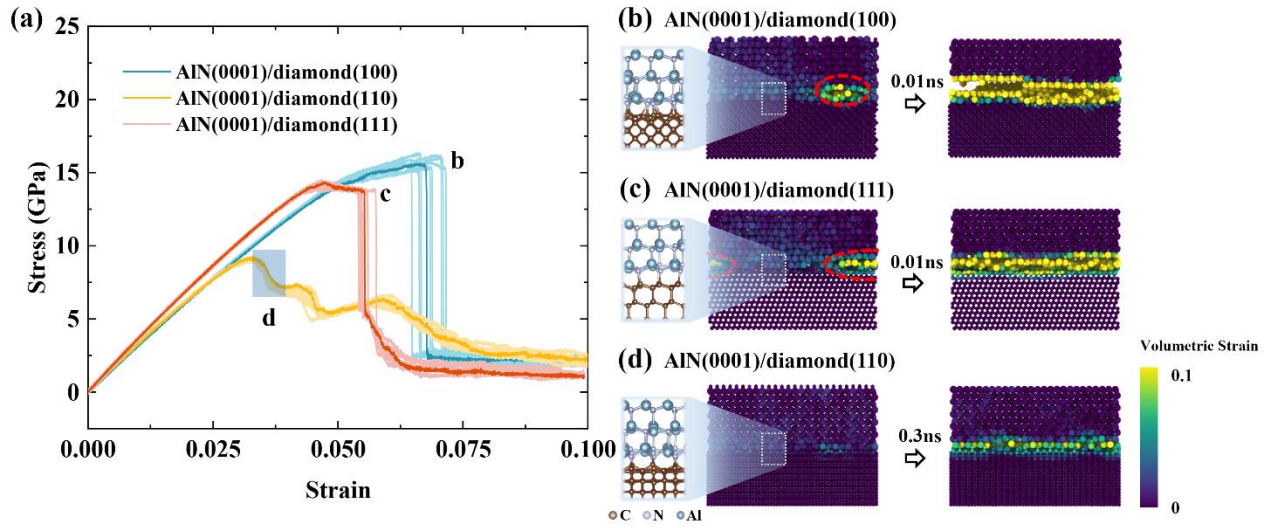

Figure 5. (a) Uniaxial stress-strain curves of heterostructures with different crystallographic orientations and the tensile fracture surfaces of (b) AlN(0001)/diamond(100), (c) AlN(0001)/diamond(111), and (d) AlN(0001)/diamond(110).

3.3. The interfacial mechanical properties of AlN/diamond heterostructures

To clarify the effect of annealing temperature on the interfacial mechanical properties, Figure 6a presents the tensile stress-strain curves for the AlN(0001)/diamond(100) heterostructures after annealing at temperatures ranging from 500 K to 1900 K. At an annealing temperature of 500 K, both the fracture strain and fracture stress increase by 5.0% and 7.6%, respectively. As the annealing temperature gradually increases, the optimization effect on the heterogeneous interfaces stabilizes.

When the annealing temperature exceeds 1300 K, the fracture strain and fracture stress remain stable at around 0.072 and 18.60 GPa, respectively. Figure 6b illustrates the average atomic potential energy of the total heterogeneous system (48744 atoms) under annealing conditions at 900 K, 1500 K, and without annealing. Notably, the average atomic potential energy decreases by 0.00202 eV/atom (after annealing at 900 K) and 0.00272 eV/atom (after annealing at 1500 K). The decrease in system potential energy means an increase in stability. In Figure 6c, distinguished by the black dotted line, it is evident that a part of atoms initially in a high-energy state (range from -7.9 eV to -7.0 eV) experiences a reduction in potential energy, falling below -7.9 eV due to the annealing treatment. By analyzing the distribution of potential energy among distinct atomic types (Figure 6d), it can be found that these atoms with decreased potential energy primarily consist of C and N atoms, and the distribution of potential energy among Al atoms demonstrates minimal variation before and after the annealing. Consequently, the annealing treatment leads to the reduction of the total potential energy by facilitating the bonding of C and N atoms at the interface and ultimately promotes the enhancement of interfacial adhesion.

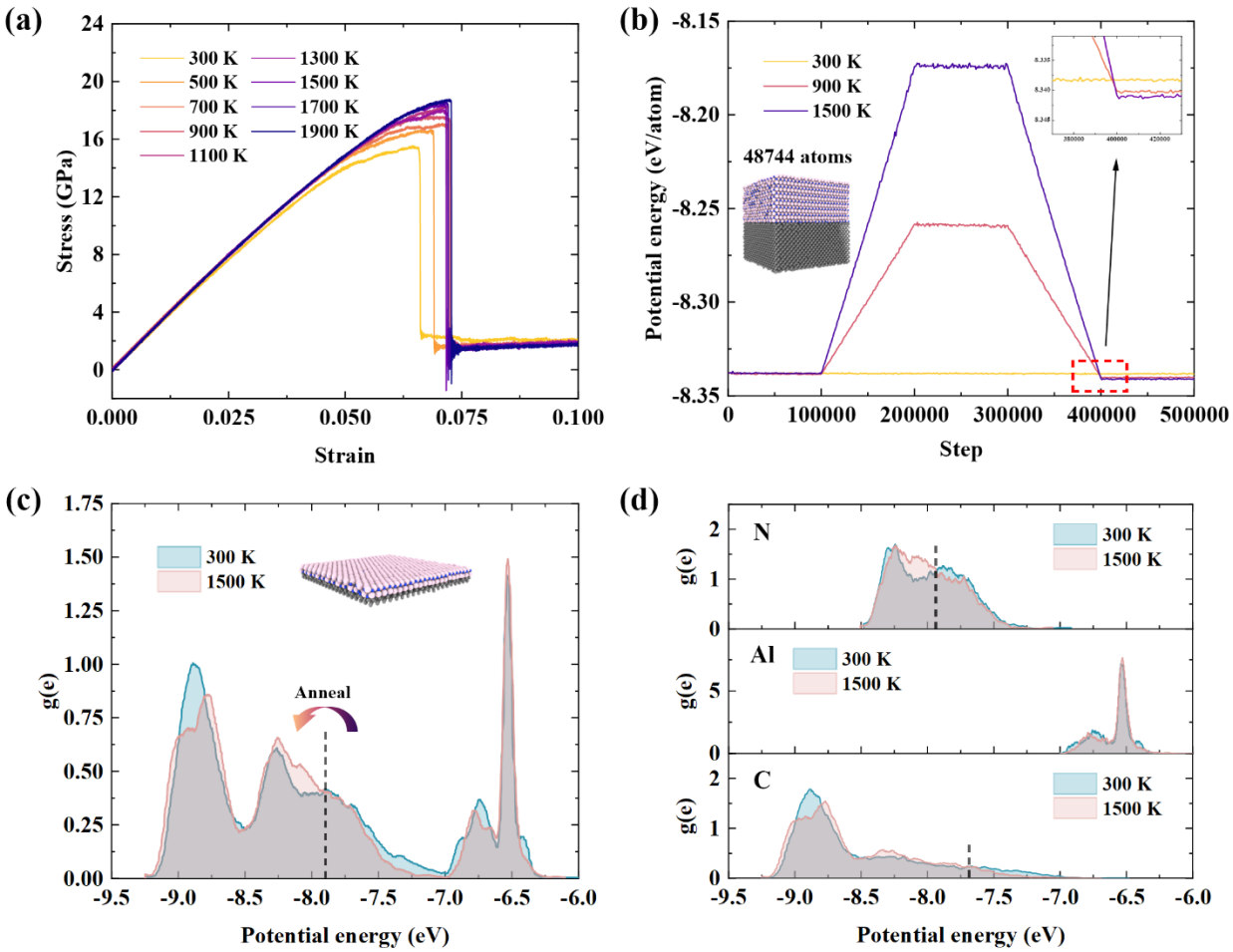

Figure 6. (a) Uniaxial stress-strain curves of AlN(0001)/diamond(100) after annealing treatments (temperature range from 500 K to 1900 K). (b) Average atomic potential energy of heterogeneous systems during the annealing simulation. (c) Potential energy distribution of atoms at the heterogeneous interface after annealing treatments, and (d) the potential energy distribution of N, Al, and C atoms within the interface.

The strain state of the heterostructure material has an important effect on the interfacial properties, whereas, in AlN/diamond heterostructures, AlN has a smaller modulus and is more prone to strain. To investigate the effect of AlN strain on the mechanical properties of the interface, the heterogeneous models consisting of an AlN substrate and a diamond nanopillar have been constructed (Figure 3c), and a fixed strain was applied to the AlN substrate in the *xy*-plane by modifying the lattice constant of AlN and controlling the boundaries of the simulation box. As shown in Figure 7a, the strains have been introduced to the AlN substrate along three different directions: the *x*-axis (AlN[$10\bar{1}0$]), the *y*-axis (AlN[$11\bar{2}0$]), and the biaxial *xy*-plane, with strain varying from 0.95 to 1.05. The size of the diamond nanopillar remains constant and the position is always in the center of the *xy* plane of the model.

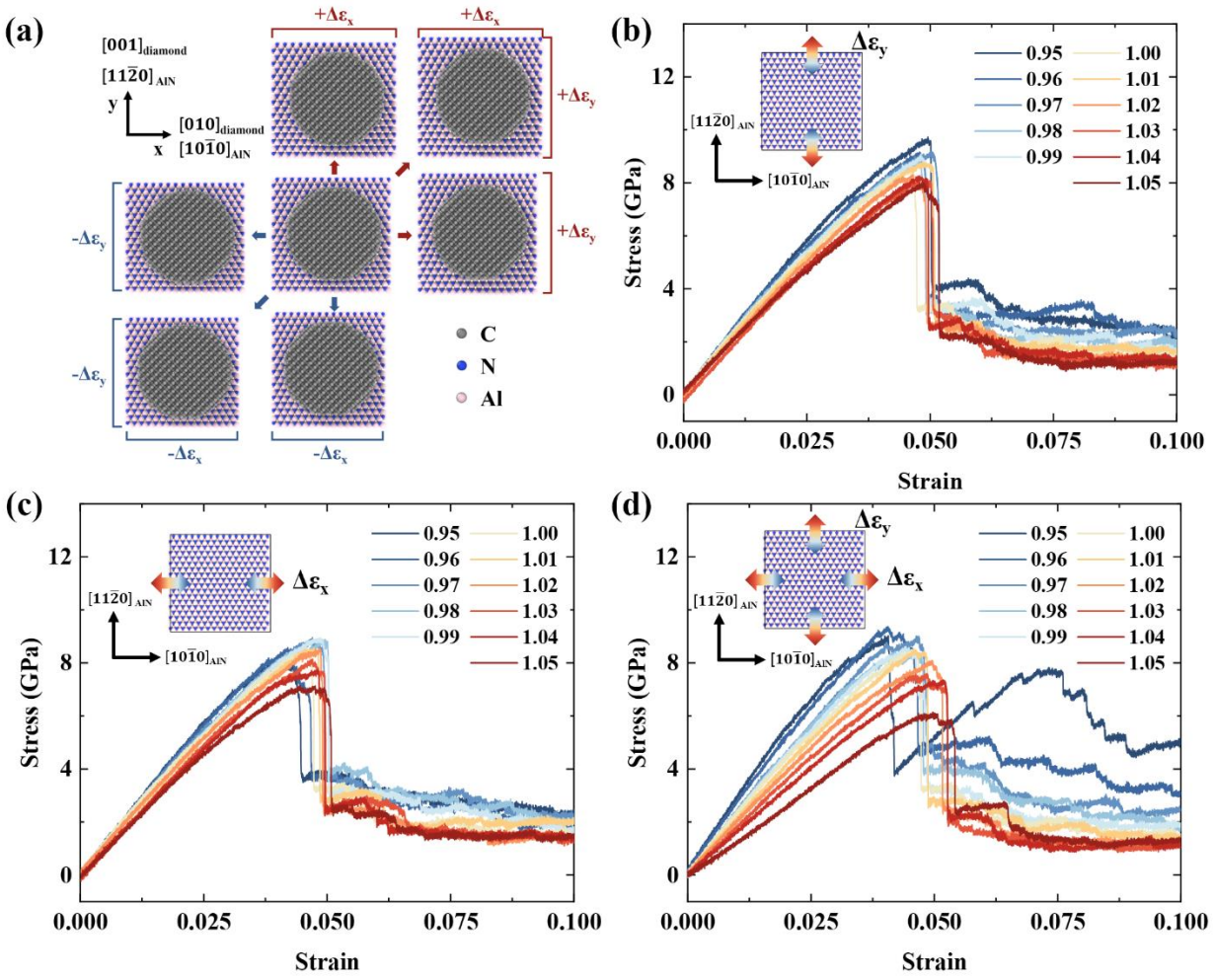

Figure 7. (a) Aerial view of the diamond nanopillar model on an AlN substrate with strain applied to the AlN substrate within the *xy* plane. (b-d) Uniaxial stress-strain curves of diamond(100)/AlN(0001) with AlN substrates under various strain conditions. The substrate strain orientations include the (b) *y*-axis (AlN[11$\bar{2}$0]), (c) *x*-axis (AlN[10$\bar{1}$0]), and (d) *xy*-plane, with a strain magnitude range of 0.95-1.05.

The tensile stress-strain curves for the heterogeneous nanopillar model are shown in Figure 7b-c. The blue lines represent AlN in a compressed state and the red lines represent AlN in a tensile state. When the substrate strain is in the *x*-axis direction (Figure 7c), whether under compression or tension, the fracture strain and fracture stress at the interface do not improve significantly, but instead both exhibit a certain decrease. When the strain of AlN substrate is along the *y*-axis (Figure 7b), compared to the unstrained state, the fracture stress increases by 10.8% at a *y*-axis strain of 0.95 (9.66 GPa), while it decreases by 8.8% at a *y*-axis strain of 1.05 (7.95 GPa). Furthermore, based on the potential energy calculation of the system before and after fracture (Figure S3), it can be found that strain engineering has an impact on the adhesion energy of the heterostructure, which is an important

influencing factor of fracture stress. As the substrate strain transitions from tensile to compressive state, a noticeable enhancement trend is observed in tensile fracture stress. Among the strains of AlN substrate along the *x*-axis or *y*-axis, compressive strain leads to a higher modulus at the heterogeneous interfaces, while tensile strain decreases the modulus. This trend becomes more pronounced under biaxial strain. When the AlN substrate is subjected to biaxial strain, the stress-strain curves exhibit significant variations (Figure 7d). As the strain state of AlN substrate changes from compression to tension, both the modulus and fracture stress of the heterostructures decrease. The maximum fracture stress at a strain of 0.95 is lower than that in the *y*-axis uniaxial strain of 0.95, and it is worth noting that the fracture stress decreases at the *x*-axis uniaxial strain of 0.95. It can be speculated that these trends in the stress-strain curves under biaxial strain are consistent with the superposition of *x*-axis and *y*-axis uniaxial strains.

The morphology and nanostructure engineering of interfaces can also play a crucial role in determining interface properties. Figure 8a shows the stress-strain curves of the models with different interface morphologies, including AlN nanopillar interface, diamond nanopillar interface and 1.5 nm roughness interface (Figure 8b-d). The model pre-processing includes annealing group (at 1500 K) and room temperature group. It can be observed that the failure mode with nanostructures is also the cleavage of AlN caused by AlN defects near the interface during the tensile process, while the rough interface exhibits smaller failure stresses. The results indicate that the fracture stress of the interface with nanostructures is greater than that of the 1.5nm roughness interface. The fracture stress of the interface with diamond nanopillar nanostructures after annealing is 14.7 GPa, which is close to the fracture stress of the flat AlN(0001)/diamond(100) interface (15.5 GPa). The fracture strains of the nanostructure interfaces are related to the volume ratio of AlN and diamond at the fracture site, so that a comparison of fracture strains is not made here. The results show that undulating surface morphology increases the contact area of the material to improve the interaction between atoms, but also makes it more prone to defects. Under both effects, the interfacial adhesion of the nanostructure interface and the roughness interface is lower than that of the ideal flat interface.

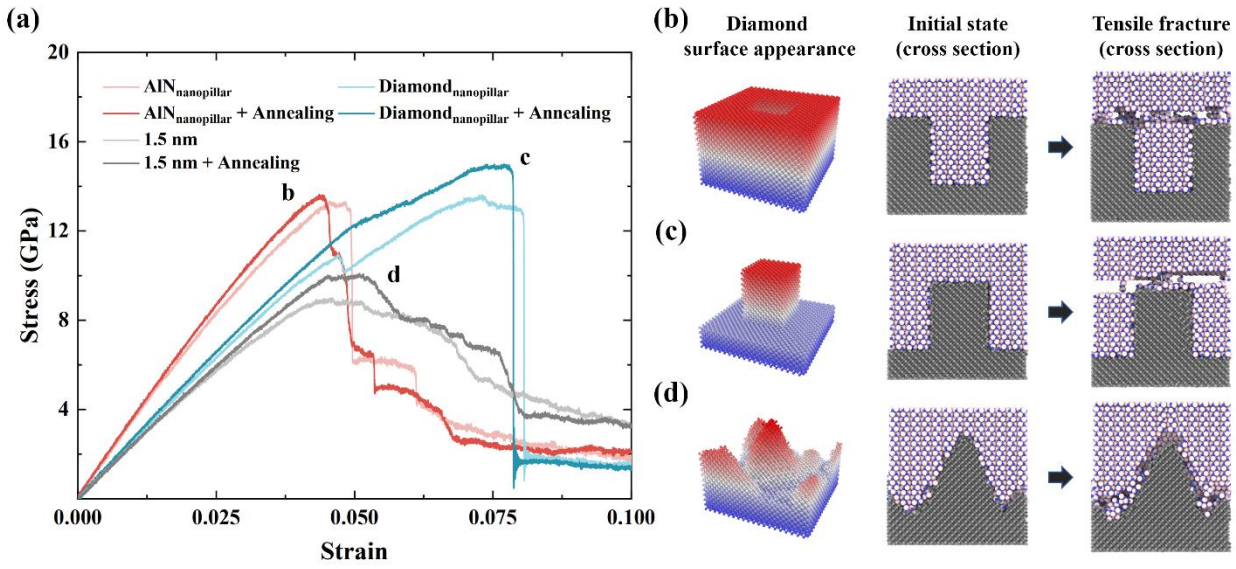

Figure 8. (a) Uniaxial stress-strain curves of AlN(0001)/diamond(100) with nanopillar and rough interface. The diamond surface appearance in the heterostructures and the model cross sections before and after tensile of (b) AlN nanopillar interface, (c) diamond nanopillar interface and (d) interface with a roughness of 1.5 nm.

Based on the above investigations on the effects of annealing treatment, AlN strain engineering, and interface morphology on interfacial adhesion in AlN/diamond heterostructures, the tensile fracture processes after adopting different optimization strategies have been summarized and calculated, and the tensile fracture stress is shown in Figure 9. The adhesion of rough interfaces can be improved by reducing roughness or introducing interfacial nanostructures. The flat interface has the largest fracture stress, which is 72.8% higher than that of the 1.5 nm roughness interface. Annealing treatment at 1500 K has a significant effect on improving the fracture stress of various interfaces. Applying a strain (0.95) to AlN along $[11\bar{2}0]$ can increase the interface fracture stress with or without annealing treatment. Combining annealing treatment and AlN strain engineering can increase the flat interface fracture strength by 17.7%.

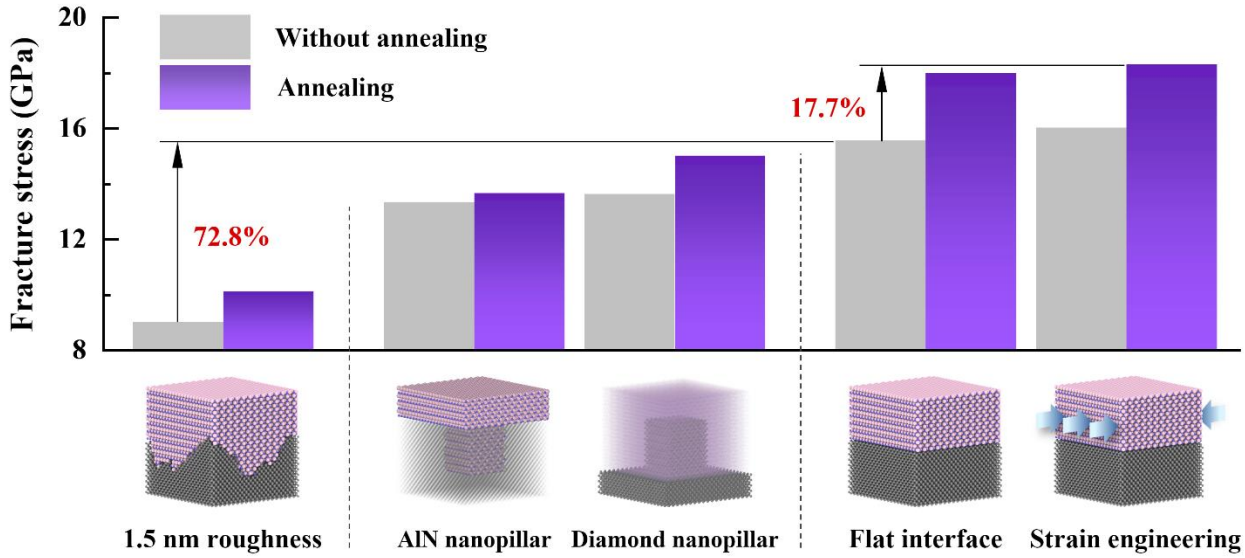

Figure 9. Fracture stress of AlN/diamond heterostructures with different interface morphologies. Gray represents the heterostructure without annealing treatment, and purple represents the heterostructure with annealing treatment at 1500 K.

4. CONCLUSIONS

In summary, based on the AlN and diamond datasets calculated by DFT, the trained NEP can effectively describe the crystal structure, tensile fracture, and crystal cleavage. By simulating and analyzing the heterogeneous tensile fracture of diamond (100), (110), (111) planes with AlN (0001), it can be found that the AlN(0001)/diamond(100) heterostructures have relatively high interfacial adhesion. The annealing treatment promotes the bonding of C and N atoms at the interface, thereby reducing the total potential energy. In addition, the strain state of AlN has an effect on the fracture strength of the interface, and appropriate strain engineering can improve the interfacial strength. Simulations of the heterostructures with rough interface and interfacial nanostructure show that the introduction of interfacial nanostructures and the reduction of roughness are effective methods to improve interfacial adhesion. The combination of roughness reduction, AlN strain engineering, and annealing treatment ultimately results in AlN/diamond heterostructures with superior and more stable interfacial mechanical properties, which may provide a promising way to address the poor adhesion at heterogeneous interfaces within the UWBG semiconductor materials.

Supporting Information

Comparison of DFT and NEP in heterostructure energy calculations; additional discussion on size effects in tensile models; calculations of interfacial adhesion energy for strain engineering heterostructures.

Declaration of Competing Interest

The authors declare that they have no known competing financial interests or personal relationships that could have appeared to influence the work reported in this paper.

Data Availability

The data that support the findings of this study are available from the corresponding author upon reasonable request.

Acknowledgements

This work was funded by the National Natural Science Foundation of China (Grant Nos. 52202045, 62004141), the Knowledge Innovation Program of Wuhan-Shuguang (Grant Nos. 2023010201020243, 2023010201020255), the Fundamental Research Funds for the Central Universities (Grant Nos. 2042023kf0112, 2042022kf1028), the Major Program (JD) of Hubei Province (Grant No. 2023BAA009), the Hubei Natural Science Foundation (Grant No. 2022CFB606), and the Open Fund of Hubei Key Laboratory of Electronic Manufacturing and Packaging Integration (Grant Nos. EMPI2024014, EMPI2023027).

References

(1) Sznajder, M. DFT-based modelling of carbon adsorption on the AlN surfaces and influence of point defects on the stability of diamond/AlN interfaces. *Diamond Relat. Mater.* **2020,** *103*, 107694, DOI: 10.1016/j.diamond.2020.107694.

(2) Wu, K.; Ma, W.; Sun, C.; Wang, Z.; Ling, L.; Chen, C. Two dimensional hole gas induced by the heterointerface of nonpolar plane AlN(1 (1)over-bar 0 0)/H-terminated (100) diamond. *Comput. Mater. Sci* **2018,** *145*, 191-196, DOI: 10.1016/j.commatsci.2018.01.007.
(3) Wu, Y. P.; Laleyan, D. A.; Deng, Z. H.; Ahn, C.; Aiello, A. F.; Pandey, A.; Liu, X. H.; Wang, P.; Sun, K.; Ahmadi, E.; Sun, Y.; Kira, M.; Bhattacharya, P. K.; Kioupakis, E.; Mi, Z. T. Controlling defect formation of nanoscale AlN: Toward efficient current conduction of ultrawide-bandgap semiconductors. *Adv. Electron. Mater.* **2020,** *6* (9), 2000337, DOI: 10.1002/aelm.202000337.
(4) Leigh, W.; Mandal, S.; Cuenca, J. A.; Wallis, D.; Hinz, A. M.; Oliver, R. A.; Thomas, E. L. H.; Williams, O. Monitoring of the initial stages of diamond growth on aluminum nitride using in situ spectroscopic ellipsometry. *ACS Omega* **2023,** *8* (33), 30442-30449, DOI: 10.1021/acsomega.3c03609.
(5) Mandal, S.; Yuan, C.; Massabuau, F.; Pomeroy, J. W.; Cuenca, J.; Bland, H.; Thomas, E.; Wallis, D.; Batten, T.; Morgan, D.; Oliver, R.; Kuball, M.; Williams, O. A. Thick, adherent diamond films on AIN with low thermal barrier resistance. *ACS Appl. Mater. Interfaces* **2019,** *11* (43), 40826-40834, DOI: 10.1021/acsami.9b13869.
(6) Wang, L.; Chen, S.; Zhang, J.; Xiao, D.; Han, K.; Ning, X.; Liu, J.; Chen, Z.; Zhou, J. Enhanced performance of 17.7 GHz SAW devices based on AlN/diamond/Si layered structure with embedded nanotransducer. *Appl. Phys. Lett.* **2017,** *111* (25), 253502 DOI: 10.1063/1.5006884.
(7) Wang, B.; Xiao, M.; Zhang, Z.; Wang, Y.; Qin, Y.; Song, Q.; Lu, G.-Q.; Ngo, K.; Zhang, Y. Chip size minimization for wide and ultrawide bandgap power devices. *IEEE Trans. Electron Devices* **2023,** *70* (2), 633-639, DOI: 10.1109/ted.2022.3232309.
(8) Donato, N.; Rouger, N.; Pernot, J.; Longobardi, G.; Udrea, F. Diamond power devices: state of the art, modelling, figures of merit and future perspective. *J. Phys. D-Appl. Phys.* **2020,** *53* (9), 093001, DOI: 10.1088/1361-6463/ab4eab.
(9) Millan, J.; Godignon, P.; Perpina, X.; Perez-Tomas, A.; Rebollo, J. A survey of wide bandgap power semiconductor devices. *IEEE Trans. Power Electron.* **2014,** *29* (5), 2155-2163, DOI: 10.1109/tpel.2013.2268900.
(10) Sun, H.; Simon, R. B.; Pomeroy, J. W.; Francis, D.; Faili, F.; Twitchen, D. J.; Kuball, M. Reducing GaN-on-diamond interfacial thermal resistance for high power transistor applications. *Appl. Phys. Lett.* **2015,** *106* (11), 111906 DOI: 10.1063/1.4913430.
(11) Hirayama, H.; Maeda, N.; Fujikawa, S.; Toyoda, S.; Kamata, N. Recent progress and future prospects of AlGaN-based high-efficiency deep-ultraviolet light-emitting diodes. *Jpn. J. Appl. Phys.* **2014,** *53* (10), 100209, DOI: 10.7567/jjap.53.100209.
(12) Saito, W.; Takada, Y.; Kuraguchi, M.; Tsuda, K.; Omura, I. Recessed-gate structure approach toward normally off high-voltage AlGaN/GaN HEMT for power electronics applications. *IEEE Trans. Electron Devices* **2006,** *53* (2), 356-362, DOI: 10.1109/ted.2005.862708.
(13) Khramtsov, I. A.; Fedyanin, D. Y. Bright single-photon emitting diodes based on the silicon-vacancy center in AlN/Diamond heterostructures. *Nanomaterials* **2020,** *10* (2), 361, DOI: 10.3390/nano10020361.
(14) Hirama, K.; Taniyasu, Y.; Kasu, M. Electroluminescence and capacitance-voltage characteristics of single-crystal n-type AlN (0001)/p-type diamond (111) heterojunction diodes. *Appl. Phys. Lett.* **2011,** *98* (1), 011908 DOI: 10.1063/1.3533380.
(15) Miskys, C. R.; Garrido, J. A.; Nebel, C. E.; Hermann, M.; Ambacher, O.; Eickhoff, M.; Stutzmann, M. AlN/diamond heterojunction diodes. *Appl. Phys. Lett.* **2003,** *82* (2), 290-292, DOI: 10.1063/1.1532545.
(16) Imura, M.; Hayakawa, R.; Watanabe, E.; Liao, M. Y.; Koide, Y.; Amano, H. Demonstration of

diamond field effect transistors by AlN/diamond heterostructure. *Phys. Status Solidi-Rapid Res. Lett.* **2011,** *5* (3), 125-127, DOI: 10.1002/pssr.201105024.
(17) Smith, E. J. W.; Piracha, A. H.; Field, D.; Pomeroy, J. W.; Mackenzie, G. R.; Abdallah, Z.; Massabuau, F. C. P.; Hinz, A. M.; Wallis, D. J.; Oliver, R. A.; Kuball, M.; May, P. W. Mixed-size diamond seeding for low-thermal-barrier growth of CVD diamond onto GaN and AlN. *Carbon* **2020,** *167*, 620-626, DOI: 10.1016/j.carbon.2020.05.050.
(18) Mu, F.; He, R.; Suga, T. Room temperature GaN-diamond bonding for high-power GaN-on-diamond devices[J]. *Scr. Mater.* **2018**, *150*: 148-151. DOI: 10.1016/j.scriptamat.2018.03.016.
(19) Liang, J.; Kobayashi, A.; Shimizu, Y.; Ohno, Y.; Kim, S.; Koyama, K.; Kasu, M.; Nagai, Y.; Shigekawa, N. Fabrication of GaN/diamond heterointerface and interfacial chemical bonding state for highly efficient device design[J]. *Adv. Mater.* **2021**, *33*(43): 2104564. DOI: 10.1002/adma.202104564.
(20) Wang, Y.; Sun, X.; Chen, Z.; Cai, Z.; Zhou, H.; Lu, T.; Shi, J. Defect-engineered epitaxial $VO_{2\pm\delta}$ in strain engineering of heterogeneous soft crystals[J]. *Sci. Adv.* **2018**, *4*(5): eaar3679. DOI: 10.1126/sciadv.aar3679.
(21) Chen, Y.; Lei, Y.; Li, Y.; Yu, Y.; Cai, J.; Chiu, M.; Rao, R.; Gu, Y.; Wang, C.; Choi, W.; Hu, H.; Wang, C.; Li, Y.; Song, J.; Zhang, J.; Qi, B.; Lin, M.; Zhang, Z.; Islam, A. E.; Maruyama, B.; Dayeh, S.; Li, L.; Yang, K.; Lo Y.; Xu. S. Strain engineering and epitaxial stabilization of halide perovskites[J]. *Nature*, **2020**, *577*(7789): 209-215. DOI: 10.1038/s41586-019-1868-x.
(22) Herklotz, A.; Rus, S. F.; Ward, T. Z. Continuously controlled optical band gap in oxide semiconductor thin films[J]. *Nano Lett.* **2016**, *16*(3): 1782-1786. DOI: 10.1021/acs.nanolett.5b04815.
(23) McMitchell, S. R. C.; Walke, A. M.; Banerjee, K,; Mertens, S,; Piao, X,; Mao, M,; Katcko, K.; Vellianitis, G.; Dal, M. V.; Lin, Y.; Bosch, G. V.; Delhougne, R.; Kar, G. S. Engineering strain and texture in ferroelectric scandium-doped aluminium nitride[J]. *ACS Appl. Electron. Mater.* **2023**, *5*(2): 858-864. DOI: 10.1021/acsaelm.2c01421.
(24) Qi, Z.; Shen, W.; Li, R.; Sun, X.; Li, L.; Wang, Q.; Wu, G.; Liang, K. AlN/diamond interface nanoengineering for reducing thermal boundary resistance by molecular dynamics simulations. *Appl. Surf. Sci.* **2023,** *615*, 156419, DOI: 10.1016/j.apsusc.2023.156419.
(25) Anupam, K. C.; Anderson, J.; Ayala, A.; Engdahl, C.; Piner, E. L.; Holtz, M. W. Heterogeneous integration of high-quality diamond on aluminum nitride with low and high seeding density. *J. Cryst. Growth* **2023,** *610*, 127172, DOI: 10.1016/j.jcrysgro.2023.127172.
(26) Khan, S.; Angeles, F.; Wright, J.; Vishwakarma, S.; Ortiz, V. H.; Guzman, E.; Kargar, F.; Balandin, A. A.; Smith, D. J.; Jena, D.; Xing, H. G.; Wilson, R. Properties for thermally conductive interfaces with wide band gap materials. *ACS Appl. Mater. Interfaces* **2022,** *14* (31), 36178-36188, DOI: 10.1021/acsami.2c01351.
(27) Shirato, T.; Hayashi, Y.; Uesugi, K.; Shojiki, K.; Miyake, H. High-temperature annealing of sputter-deposited AlN on (001) diamond substrate. *Phys. Status Solidi B-Basic Solid State Phys.* **2020,** *257* (2), 1900447, DOI: 10.1002/pssb.201900447.
(28) Hirama, K.; Taniyasu, Y.; Kasu, M. Heterostructure growth of a single-crystal hexagonal AlN(0001) layer on cubic diamond (111) surface. *J. Appl. Phys.* **2010,** *108* (1), 013528, DOI: 10.1063/1.3452362.
(29) Choudhary, K.; Liang, T.; Mathew, K.; Revard, B.; Chernatynskiy, A.; Phillpot, S. R.; Hennig, R. G.; Sinnott, S. B. Dynamical properties of AIN nanostructures and heterogeneous interfaces predicted using COMB potentials. *Comput. Mater. Sci* **2016,** *113*, 80-87, DOI: 10.1016/j.commatsci.2015.11.025.
(30) Vashishta, P.; Kalia, R. K.; Nakano, A.; Rino, J. P.; Collaboratory Adv Comp, S. Interaction

potential for aluminum nitride: A molecular dynamics study of mechanical and thermal properties of crystalline and amorphous aluminum nitride. *J. Appl. Phys.* **2011,** *109* (3), 033514, DOI: 10.1063/1.3525983.
(31) Tungare, M.; Shi, Y. F.; Tripathi, N.; Suvarna, P.; Shahedipour-Sandvik, F. A Tersoff-based interatomic potential for wurtzite AlN. *Phys. Status Solidi A-Appl. Mat.* **2011,** *208* (7), 1569-1572, DOI: 10.1002/pssa.201001086.
(32) Sinnott, S. B.; Shenderova, O. A.; White, C. T.; Brenner, D. W. Mechanical properties of nanotubule fibers and composites determined from theoretical calculations and simulations. *Carbon* **1998,** *36* (1-2), 1-9, DOI: 10.1016/s0008-6223(97)00144-9.
(33) Erhart, P.; Albe, K. Analytical potential for atomistic simulations of silicon, carbon, and silicon carbide. *Phys. Rev. B* **2005,** *71* (3), 035211, DOI: 10.1103/PhysRevB.71.035211.
(34) Fan, Z. Y.; Wang, Y. Z.; Ying, P. H.; Song, K. K.; Wang, J. J.; Wang, Y.; Zeng, Z. Z.; Ke, X.; Lindgren, E.; Rahm, J. M.; Gabourie, A. J.; Liu, J. H.; Dong, H. K.; Wu, J. Y.; Yue, C.; Zheng, Z.; Jian, S.; Erhart, P.; Su, Y. J.; Ala-Nissila, T. GPUMD: A package for constructing accurate machine-learned potentials and performing highly efficient atomistic simulations. *J. Chem. Phys.* **2022,** *157*, 114801, DOI: 10.1063/5.0106617.
(35) Zhao, R.; Wang, S. C.; Kong, Z. Z.; Xu, Y. L.; Fu, K.; Peng, P.; Wu, C. L. Development of a neuroevolution machine learning potential of Pd-Cu-Ni-P alloys. *Mater. Des.* **2023,** *231*, 112012, DOI: 10.1016/j.matdes.2023.112012.
(36) Zhang, L. F.; Wang, H.; Car, R.; Weinan, E. Phase diagram of a deep potential water model. *Phys. Rev. Lett.* **2021,** *126* (23), 236001, DOI: 10.1103/PhysRevLett.126.236001.
(37) Deringer, V. L.; Csányi, G. Machine learning based interatomic potential for amorphous carbon. *Phys. Rev. B* **2017,** *95* (9), 094203, DOI: 10.1103/PhysRevB.95.094203.
(38) Fan, Z. Y. Improving the accuracy of the neuroevolution machine learning potential for multi-component systems. *Journal of Physics-Condensed Matter* **2022,** *34* (12), 125902, DOI: 10.1088/1361-648X/ac462b.
(39) Fan, Z. Y.; Zeng, Z. Z.; Zhang, C. Z.; Wang, Y. Z.; Song, K. K.; Dong, H. K.; Chen, Y.; Nissila, T. A. Neuroevolution machine learning potentials: Combining high accuracy and low cost in atomistic simulations and application to heat transport. *Phys. Rev. B* **2021,** *104* (10), 104309, DOI: 10.1103/PhysRevB.104.104309.
(40) Fan, Z. Y.; Chen, W.; Vierimaa, V.; Harju, A. Efficient molecular dynamics simulations with many-body potentials on graphics processing units. *Comput. Phys. Commun.* **2017,** *218*, 10-16, DOI: 10.1016/j.cpc.2017.05.003.
(41) Daw, M. S.; Baskes, M. I. Embedded-atom method - derivation and application to impurities, surfaces, and other defects in metals. *Phys. Rev. B* **1984,** *29* (12), 6443-6453, DOI: 10.1103/PhysRevB.29.6443.
(42) Kresse, G.; Furthmuller, J. Efficient iterative schemes for ab initio total-energy calculations using a plane-wave basis set. *Phys. Rev. B* **1996,** *54* (16), 11169-11186, DOI: 10.1103/PhysRevB.54.11169.
(43) Kresse, G.; Hafner, J. Abinitio molecular-dynamics for liquid-metals. *Phys. Rev. B* **1993,** *47* (1), 558-561, DOI: 10.1103/PhysRevB.47.558.
(44) Perdew, J. P.; Burke, K.; Ernzerhof, M. Generalized gradient approximation made simple. *Phys. Rev. Lett.* **1996,** *77* (18), 3865-3868, DOI: 10.1103/PhysRevLett.78.1396.
(45) Blochl, P. E. Projector augmented-wave method. *Phys. Rev. B* **1994,** *50* (24), 17953-17979, DOI: 10.1103/PhysRevB.50.17953.
(46) Bernetti, M.; Bussi, G. Pressure control using stochastic cell rescaling. *J. Chem. Phys.* **2020,** *153* (11), 114107, DOI: 10.1063/5.0020514.

(47) Stukowski, A. Visualization and analysis of atomistic simulation data with OVITO-the Open Visualization Tool. *Modell. Simul. Mater. Sci. Eng.* **2010,** *18* (1), 015012, DOI: 10.1088/0965-0393/18/1/015012.
(48) Nie, A. M.; Bu, Y. Q.; Li, P. H.; Zhang, Y. Z.; Jin, T. Y.; Liu, J. B.; Su, Z.; Wang, Y. B.; He, J. L.; Liu, Z. Y.; Wang, H. T.; Tian, Y. J.; Yang, W. Approaching diamond's theoretical elasticity and strength limits. *Nat. Commun.* **2019,** *10*, 5533, DOI: 10.1038/s41467-019-13378-w.
(49) Telling, R. H.; Pickard, C. J.; Payne, M. C.; Field, J. E. Theoretical strength and cleavage of diamond. *Phys. Rev. Lett.* **2000,** *84* (22), 5160-5163, DOI: 10.1103/PhysRevLett.84.5160.
(50) Zhang, R. F.; Sheng, S. H.; Veprek, S. First principles studies of ideal strength and bonding nature of AIN polymorphs in comparison to TiN. *Appl. Phys. Lett.* **2007,** *91* (3), 031906, DOI: 10.1063/1.2759265.
(51) Wright, A. F. Elastic properties of zinc-blende and wurtzite AlN, GaN, and InN. *J. Appl. Phys.* **1997,** *82* (6), 2833-2839, DOI: 10.1063/1.366114.